Eur. Phys. J. B (2021) 94:231
https://doi.org/10.1140/epjb/s10051-021-00226-4

THE EUROPEAN PHYSICAL JOURNAL B

Topical Review - Computational Methods

Multiple timescale molecular dynamics with very large time steps: avoidance of resonances

C. R. A. Abreu[1,a] and M. E. Tuckerman[2,3,4,b]

[1] Chemical Engineering Department, Escola de Química, Universidade Federal do Rio de Janeiro, Rio de Janeiro, RJ 21941-909, Brazil
[2] Department of Chemistry, New York University, New York 10003, NY, USA
[3] Courant Institute of Mathematical Sciences, New York University, New York 10012, NY, USA
[4] NYU-ECNU Center for Computational Chemistry at NYU Shanghai, Shanghai 200062, China

Received 4 August 2021 / Accepted 11 October 2021 / Published online 29 November 2021

Abstract. Reversible multiple timescale (MTS) integration algorithms have long been recognized as a straightforward way to increase efficiency and extend accessible timescales in molecular dynamics simulations without altering the ensemble distribution sampled. MTS methods are based on the idea that interatomic forces in a system drive motion on numerous timescales, and by decomposing force components according to these timescales and assigning an individual time step to each one, fast, computationally cheaper forces are evaluated more frequently than the slow, expensive forces. As it happens, the largest time step that can be employed in standard MTS methods is fundamentally limited by so-called resonance artifacts that originate in the fastest timescales. Thus, while it should be possible to assign the slowest timescales very large time steps approaching 100 fs in, for example, fully atomistic simulations, resonances impose a practical limit on this step size to around 5–10 fs, which allows for useful but only modest savings in computational overhead. This article will review the basic MTS approach and the origin of resonances and then will provide a perspective on how to solve the resonance problem for molecular dynamics simulations in different ensembles, showing how both statistical and dynamical properties can be generated with very large time steps.

1 Introduction

Multiple timescale (MTS) integration [1–3] is broadly recognized as a straightforward and effective approach to enhancing the efficiency and accessible timescales of molecular dynamics (MD) simulations without affecting the sampling of a chosen statistical ensemble. In classical MD, MTS algorithms allow the most expensive computations, typically associated with the evaluation of slowly varying long-range van der Waals and electrostatic components of a force field, to be performed less frequently than cheaper, more rapidly varying, bonded components. When a simulation is performed for the purpose of computing statistical ensemble averages, such as distribution functions, free energy differences, or other thermodynamic observables, then the maximum benefit afforded by MTS algorithms is achieved when the largest time step can be matched to the correlation time of the system dynamics (i.e. the sampling period required to obtain a series of uncorrelated configurations). Although this is theoretically possible in certain situations, resonance artifacts [4–6] limit the maximum attainable step size in a MTS run, thus inhibiting MTS algorithms from delivering maximal gains. Numerical resonances arise within MTS integration algorithms at specific values of the large time step, at which slow and fast motions "resonate" numerically, causing a significant degradation in energy conservation and integration accuracy. These resonant time steps are roughly determined by the period of the fast motion.

Over the last few decades, several schemes to circumvent resonances have been introduced. One such approach, known as the mollified impulse method [7,8], consists in modifying the slow terms in the potential energy function in such a way that the corresponding forces are evaluated at coordinates that are averaged along auxiliary trajectories determined by the fast part of the potential. A related method employs a generalized Langevin equation with a "designer" colored-noise memory kernel engineered to mollify high-frequency components of the fast motion [9]. Methods of this type allow for notable gains in the large time step and, importantly, largely preserve long timescale dynamics. If the goal of a simulation is to sample an ensemble distribution and generate equilibrium properties, very sub-

[a] e-mail: abreu@eq.ufrj.br
[b] e-mail: mark.tuckerman@nyu.edu (corresponding author)

stantial gains in the large time step are possible using an approach that alters the dynamics via the introduction of a set of isokinetic constraints. These constraints couple the physical phase-space variables to a set of auxiliary (extended phase-space) variables that modulate fluctuations in the instantaneous kinetic energy and, if desired, the virial, to maintain a target temperature and/or pressure [10–13]. The basic technique consists in pairing the velocity of each physical degree of freedom in the system with a set of extended phase-space velocities and coupling a thermostat individually to each such pair. The combined kinetic energy of each physical velocity and corresponding auxiliary velocity is then fixed by a non-holonomic constraint. In this way, the kinetic energy of any physical mode can never exceed a prescribed value and, consequently, avoids resonances and instabilities. This procedure can be shown to produce a kind of microcanonical distribution of velocities and a proper canonical or isothermal–isobaric distribution of coordinates [10–13]. The method was originally formulated [10–12] with deterministic thermostats [14] for canonical sampling and subsequently reformulated [13] with stochastic thermostats [15,16]. In the latter case, it is known as the SIN(R) method, *i.e.,* Stochastic Isokinetic Nosé–Hoover (RESPA) [13]. These approaches allow large time steps as large as 100 fs in atomistic simulations to be achieved.

Recently, we introduced a Hamiltonian-based resonance-free approach [17] that samples the same velocity distribution of the massive isokinetic framework without imposing constraints or introducing extended phase-space velocities apart from those used for standard thermostatting schemes such as Nosé–Hoover dynamics [18,19], Nosé–Hoover chains [14], or Nosé–Hoover–Langevin dynamics [16].

The method consists in replacing the kinetic energy term in the system Hamiltonian by a new momentum-dependent function chosen to restrict the velocities to lie within a finite range, which we refer to as *regulation*. The potential energy part of the Hamiltonian remains unchanged, and, thus, the coordinate-dependent part of the canonical distribution is properly generated.

In this paper, we will briefly review the standard symplectic MTS scheme known as reversible RESPA (reference-system propagator algorithm), and we will discuss how resonances arise. We will then review the incorporation of isokinetic constraints as a solution to the resonance problem and then show how to reformulate this approach within a Hamiltonian framework. Using this new Hamiltonian, we will extend the regulated dynamics scheme for simulations in the isothermal–isobaric ensemble that allow very large time steps to be employed. After this development, we will describe an alternative scheme based on the colored-noise generalized Langevin approach [20]. We will conclude with a summary and a discussion about possible next steps in this topic.

2 Multiple timescale molecular dynamics

In this section, we provide a brief review of the basic symplectic Hamiltonian MTS algorithm to introduce the notation and formalism that will be used throughout this article. Consider an N-particle system with coordinates $\mathbf{r}_1, ..., \mathbf{r}_N \equiv \mathbf{r}$, momenta $\mathbf{p}_1, ..., \mathbf{p}_N \equiv \mathbf{p}$, mass $m_1, ..., m_N$, which are the elements of an $N \times N$ diagonal mass matrix M. In any configuration, the particles exert forces $\mathbf{F}_1(\mathbf{r}), ..., \mathbf{F}_N(\mathbf{r}) \equiv \mathbf{F}(\mathbf{r})$ on each other, and these forces are derived from a potential energy function $U(\mathbf{r})$ via the usual relation $\mathbf{F}(\mathbf{r}) = -\partial U/\partial \mathbf{r}$. Thus, the Hamiltonian for the system is

$$\mathcal{H}(\mathbf{r}, \mathbf{p}) = \frac{1}{2}\mathbf{p}^{\mathrm{T}} \cdot \mathrm{M}^{-1} \cdot \mathbf{p} + U(\mathbf{r}) \tag{1}$$

Defining the anti-self-adjoint Liouville operator $\mathcal{L}$ as

$$\mathcal{L} = \mathrm{M}^{-1}\mathbf{p} \cdot \frac{\partial}{\partial \mathbf{r}} + \mathbf{F}(\mathbf{r}) \cdot \frac{\partial}{\partial \mathbf{p}} \tag{2}$$

Hamilton's equations of motion

$$\begin{aligned} \dot{\mathbf{r}} &= \frac{\partial \mathcal{H}}{\partial \mathbf{p}} = \mathrm{M}^{-1}\mathbf{p} \\ \dot{\mathbf{p}} &= -\frac{\partial \mathcal{H}}{\partial \mathbf{r}} = -\frac{\partial U}{\partial \mathbf{r}} = \mathbf{F}(\mathbf{r}) \end{aligned} \tag{3}$$

can be written compactly as

$$\dot{\mathbf{r}} = \mathcal{L}\mathbf{r}, \qquad \dot{\mathbf{p}} = \mathcal{L}\mathbf{p}. \tag{4}$$

If we define the full phase space vector $\mathrm{x} = (\mathbf{r}, \mathbf{p})$, then for an initial condition x(0), Eq. (4) has the formal solution $\mathrm{x}(t) = \exp(\mathcal{L}t)\mathrm{x}(0)$. The unitary operator $\exp(\mathcal{L}t)$, known as the *classical propagator*, cannot be evaluated in closed form for general nonlinear many-body systems. However, for a small time increment, Δt, the MD time step, the propagator can be approximately factorized using the Trotter theorem:

$$e^{\mathcal{L}\Delta t} = e^{\mathcal{L}_2 \Delta t/2} e^{\mathcal{L}_1 \Delta t} e^{\mathcal{L}_2 \Delta t/2} + \mathcal{O}\left(\Delta t^3\right), \tag{5}$$

where

$$\mathcal{L}_1 = \mathrm{M}^{-1}\mathbf{p} \cdot \frac{\partial}{\partial \mathbf{r}}, \qquad \mathcal{L}_2 = \mathbf{F}(\mathbf{r}) \cdot \frac{\partial}{\partial \mathbf{p}}. \tag{6}$$

Application of the operator product in Eq. (5) on an initial phase space vector x(0) yields the standard velocity Verlet algorithm [2,21], which confirms that the algorithm is symplectic and phase-space volume-preserving. The size of the time step that can be employed is dictated by the most rapidly varying forces in a system, which, in classical atomistic models of molecular systems, for example, are bond-stretching, angle-bending, and torsional forces. Strong timescale separations also

occur in other simulation problems including path integral molecular dynamics [22,23], in which pseudoparticles or "beads" are connected to their neighbors by stiff harmonic springs, and coarse-grained models of polymers and biological macromolecules, [24–27] in which interaction sites are also coupled by stiff springs. In many of these examples, non-bonded interactions can also be decomposed into rapidly varying, strong short-range collision forces and slowly varying, weak, long-range forces, thereby leading to another timescale separation. MTS integrators aim to increase the efficiency of simulations characterized by such timescale separations by assigning appropriate time steps to different force components based on their associated timescale.

To introduce the concept of an MTS integrator, suppose the forces can be decomposed into two components according to $\mathbf{F} = \mathbf{F}_{\mathrm{f}} + \mathbf{F}_{\mathrm{s}}$, where $\mathbf{F}_{\mathrm{f}}$ and $\mathbf{F}_{\mathrm{s}}$ are fast and slow components, respectively. If the computational overhead associated with the evaluation of $\mathbf{F}_{\mathrm{f}}$ is much lower than that needed to evaluate $\mathbf{F}_{\mathrm{s}}$, then the efficiency of a simulation can be increased if a small time step $\delta t = \Delta t/n_{\mathrm{ref}}$, where n_{ref} is a positive integer, is used to integrate motion due to $\mathbf{F}_{\mathrm{f}}$ while Δt is used to integrate motion due to $\mathbf{F}_{\mathrm{s}}$. This can be done within a symplectic pattern following the framework of Eq. (5) by introducing the following decomposition of the Liouville operator:

$$\mathcal{L} = \mathcal{L}_{\mathrm{ref}} + \mathcal{L}_{\mathrm{s}}, \tag{7}$$

where

$$\mathcal{L}_{\mathrm{ref}} = \mathrm{M}^{-1}\mathbf{p}\cdot\frac{\partial}{\partial \mathbf{r}} + \mathbf{F}_{\mathrm{f}}(\mathbf{r})\cdot\frac{\partial}{\partial \mathbf{p}}, \qquad \mathcal{L}_{\mathrm{s}} = \mathbf{F}_{\mathrm{s}}(\mathbf{r})\cdot\frac{\partial}{\partial \mathbf{p}}. \tag{8}$$

Here, $\mathcal{L}_{\mathrm{ref}}$ defines a "reference system" propagator, which constitutes a full Hamiltonian system in which only the fast forces $\mathbf{F}_{\mathrm{f}}$ are present. If the full propagator $\exp(\mathcal{L}\Delta t)$ is now factorized according to

$$e^{\mathcal{L}\Delta t} = e^{\mathcal{L}_{\mathrm{s}}\Delta t/2} e^{\mathcal{L}_{\mathrm{ref}}\Delta t} e^{\mathcal{L}_{\mathrm{s}}\Delta t/2} + \mathcal{O}\left(\Delta t^3\right), \tag{9}$$

then Δt can be chosen to match the variation of the slow force $\mathbf{F}_{\mathrm{s}}$. In this factorization, the operator $\exp(\mathcal{L}_{\mathrm{ref}}\Delta t)$ cannot be evaluated in closed form except for very simple cases, *e.g.*, a separable system of harmonic oscillators. Therefore, in general, it is necessary to factorize $\exp(\mathcal{L}_{\mathrm{ref}}\Delta t)$, which is where the small time step δt is used. Defining the operators

$$\mathcal{L}_{\mathrm{ref},1} = \mathrm{M}^{-1}\mathbf{p}\cdot\frac{\partial}{\partial \mathbf{r}}, \qquad \mathcal{L}_{\mathrm{ref},2} = \mathbf{F}_{\mathrm{f}}(\mathbf{r})\cdot\frac{\partial}{\partial \mathbf{p}}, \tag{10}$$

we can recast Eq. (9) as

$$e^{\mathcal{L}\Delta t} = e^{\mathcal{L}_{\mathrm{s}}\Delta t/2}\left[e^{\mathcal{L}_{\mathrm{ref},2}\delta t/2} e^{\mathcal{L}_{\mathrm{ref},1}\delta t} e^{\mathcal{L}_{\mathrm{ref},2}\delta t/2}\right]^{n_{\mathrm{ref}}} e^{\mathcal{L}_{\mathrm{s}}\Delta t/2}. \tag{11}$$

The first step in the action of Eq. (11) on a phase-space vector x is a simple translation of momenta $\mathbf{p} \leftarrow \mathbf{p} + \Delta t\mathbf{F}_{\mathrm{s}}/2$. The output of this step is then used to seed n_{ref} steps of velocity Verlet using only the fast force $\mathbf{F}_{\mathrm{f}}$ and a time step δt. Finally, the output of this step is then used to perform one last momentum update identical to the first, *i.e.*, $\mathbf{p} \leftarrow \mathbf{p} + \Delta t\mathbf{F}_{\mathrm{s}}/2$ but with an updated slow force. Thus, the computational costly slow force $\mathbf{F}_{\mathrm{s}}$ only needs to be evaluated once for each of n_{ref} evaluations of the fast force $\mathbf{F}_{\mathrm{f}}$. If the cost of evaluating $\mathbf{F}_{\mathrm{f}}$ is negligible compared to the evaluation of the slow force, then the gain in efficiency is approximately equal to n_{ref}. From Eq. (11), it is easy to see how the framework can be extended to incorporate additional time steps when the forces can be further decomposed based on additional timescales.

The formalism in Eq. (11) can be extended beyond the two timescales to include as many timescales as one might wish to treat in a given system. Unfortunately, it is now well-established that MTS integrators hit a practical limit due to numerical resonance phenomena. When the fast motion in a system is characterized by a spectrum of high frequencies, then such resonances can occur at large time steps chosen to be multiples of the periods associated with these frequencies, indicating that resonances are possible at a dense set of such periods. As with ordinary resonances, the signature of a resonance is buildup of energy in a set of modes, causing a degradation in energy conservation and a loss of accuracy in the simulation [5,6,28]. Methods that have been proposed for staving off resonance involve mollifying these high frequencies [4,7,9] while preserving long-time dynamics. More aggressive techniques that effectively eliminate resonances via kinetic energy constraints or modification of the Hamiltonian in an extended phase space sacrifice dynamics in favor of preserving the ensemble distribution and the associated sampling generated by the MD algorithm [12,13,17,29–31]. In the proceeding sections of this paper, we will discuss resonance-avoiding methods for MTS integration in molecular dynamics and the choice of methods that should be made when dynamical quantities are desired or when equilibrium distributions are needed. We will show how the methods of Refs. [12,13,17], which are designed to generate a canonical distribution, can be adapted for the isothermal–isobaric ensemble.

3 Stochastic-isokinetic and regulated dynamics algorithms

The basic idea of isokinetic methods is to couple each physical velocity to a set of L velocity-like variables in an extended phase space via a (non-holonomic) constraint on the total kinetic energy of this set of $L+1$ variables. If v_α is the physical velocity of the αth degree of freedom ($\alpha = 1, ..., 3N$) and $v_{k,\alpha}$, $k = 1, ..., L$ is the set of extended phase-space velocities coupled to v_α, then the constraint takes the form

$$m_\alpha v_\alpha^2 + \frac{L}{L+1}\sum_{k=1}^{L} Q_\alpha v_{k,\alpha}^2 = Lk_{\mathrm{B}}T, \tag{12}$$

where m_α is the physical mass, Q_α is a fictitious mass-like parameter associated with $v_{k,\alpha}$, and T is the physical temperature. This constraint can be implemented in Hamilton's equations of motion via Gauss' principle of least constraint [32] with a Lagrange multiplier λ_α:

$$\begin{aligned}\dot{r}_\alpha &= v_\alpha \\ \dot{v}_\alpha &= \frac{F_\alpha(\mathbf{r})}{m_\alpha} - \lambda_\alpha v_\alpha \\ \dot{v}_{k,\alpha} &= -\lambda_\alpha v_{k,\alpha}.\end{aligned} \tag{13}$$

In its original formulation by Minary et al. [12], these equations were coupled to a set of L Nosé–Hoover chain thermostats [14], while a subsequent formulation by Leimkuhler et al. replaced the Nosé–Hoover chains with Nosé–Hoover–Langevin thermostats [16] so that ergodicity could be proved [13]. When this is done, the extended velocities $v_{k,\alpha}$ are augmented to be a set of two velocities, denoted $v_{k,\alpha}$ and $u_{k,\alpha}$, and the equations of motion, which are now stochastic in nature, take the form

$$\begin{aligned}\mathrm{d}r_\alpha &= v_\alpha \mathrm{d}t \\ \mathrm{d}v_\alpha &= \frac{F_\alpha(\mathbf{r})}{m_\alpha}\mathrm{d}t - \lambda_\alpha v_\alpha \mathrm{d}t \\ \mathrm{d}v_{k,\alpha} &= -\lambda_\alpha v_{k,\alpha}\mathrm{d}t - u_{k,\alpha} v_{k,\alpha}\mathrm{d}t \\ \mathrm{d}u_{k,\alpha} &= \frac{G(v_{k,\alpha})}{\mathcal{Q}_\alpha}\mathrm{d}t - \gamma_\alpha u_{k,\alpha}\mathrm{d}t + \sigma_\alpha \mathrm{d}w_\alpha,\end{aligned} \tag{14}$$

where γ_α is a friction parameter, $G(v_{k,\alpha}) = Q_\alpha v_{k,\alpha}^2 - k_\mathrm{B}T$, $\mathcal{Q}_\alpha$ is a thermostat mass-like parameter, $\sigma_\alpha = \sqrt{2\gamma_\alpha k_\mathrm{B}T/\mathcal{Q}_\alpha}$, $\mathrm{d}w_\alpha$ is the infinitesimal Wiener process. The Lagrange multiplier is obtained by differentiating Eq. (12) once with respect to time, substituting into Eq. (14), and solving for the multiplier. This procedure yields

$$\lambda_\alpha = \frac{v_\alpha F_\alpha(\mathbf{r}) - \frac{L}{L+1}\sum_{k=1}^{L} Q_\alpha v_{k,\alpha}^2 u_{k,\alpha}}{m_\alpha v_\alpha^2 + \frac{L}{L+1}\sum_{k=1}^{L} Q_\alpha v_{k,\alpha}^2}. \tag{15}$$

The full set of equations of motion can be obtained by substituting the expression for λ_α in Eq. (15) back into Eq. (14). The distribution sampled by Eq. (14) can be shown to be canonical in the physical configuration space, *i.e.,* $\rho(\mathbf{r}) \propto \exp(-\beta U(\mathbf{r}))$ [13]. The velocity distribution for each degree of freedom is a δ-function expressing the fact that Eq. (12) is satisfied. Because of the constraint, Eq. (14) ensure that the maximum value of the velocity $|v_\alpha|$ is $\sqrt{Lk_\mathrm{B}T/m_\alpha}$. In this way, energy is prevented from building up in any particular degree of freedom, thus avoiding resonances when Eq. (14) are integrated via MTS algorithms [13].

It is important to note that, even in the absence of the thermostat coupling, when Gauss' principle is applied to the kinetic energy constraint in Eq. (12), the resulting equations of motion are non-Hamiltonian. Recently, Abreu and Tuckerman showed that the isokinetic constraint could be reformulated via a Hamiltonian [17], thus increasing the flexibility of the scheme and rendering the task of designing MTS integrators considerably simpler. To see how this can be done, consider the following Hamiltonian:

$$\mathcal{H}(\mathbf{r},\mathbf{p}) = \sum_{\alpha=1}^{3N} m_\alpha c_\alpha^2 \ln\cosh\left(\frac{p_\alpha}{m_\alpha c_\alpha}\right) + U(\mathbf{r}), \tag{16}$$

where c_α is a parameter whose meaning will become clear shortly. If Hamilton's equations are derived from Eq. (16), the result is

$$\begin{aligned}\dot{r}_\alpha &= \frac{\partial \mathcal{H}}{\partial p_\alpha} = c_\alpha \tanh\left(\frac{p_\alpha}{m_\alpha c_\alpha}\right) = v_\alpha \\ \dot{p}_\alpha &= -\frac{\partial \mathcal{H}}{\partial r_\alpha} = -\frac{\partial U(\mathbf{r})}{\partial r_\alpha}.\end{aligned} \tag{17}$$

With this Hamiltonian, the usual classical-mechanical relation $v_\alpha = p_\alpha/m_\alpha$ between velocity and momentum no longer holds. Rather, the relation is given in the first line of Eq. (17), and this relation tells us that the maximum value of $|v_\alpha|$ is c_α. Thus, as in the isokinetic scheme, for constant-temperature ensembles we define [17]

$$c_\alpha = \sqrt{\frac{Lk_\mathrm{B}T}{m_\alpha}}, \tag{18}$$

where L is no longer restricted to integer values.

Because Eq. (16) differs from a standard Hamiltonian in the kinetic energy part only, if Eq. (17) are coupled to a thermostat, it becomes readily apparent that the phase-space distribution generated is a Boltzmann distribution in the physical coordinates. For example, if Nosé–Hoover–Langevin thermostat is used, the equations of motion would take the form

$$\begin{aligned}\mathrm{d}r_\alpha &= v_\alpha(p_\alpha)\mathrm{d}t \\ \mathrm{d}p_\alpha &= \left(F_\alpha(\mathbf{r}) - u_\alpha p_\alpha\right)\mathrm{d}t \\ \mathrm{d}u_\alpha &= \frac{p_\alpha v_\alpha(p_\alpha) - k_\mathrm{B}T}{\mathcal{Q}_\alpha}\mathrm{d}t - \gamma_\alpha u_\alpha \mathrm{d}t + \sigma_\alpha \mathrm{d}w_\alpha\end{aligned} \tag{19}$$

with function $v_\alpha(p_\alpha)$ defined in Eq. (17). MTS integration algorithms for Eq. (19) were described in detail by Abreu and Tuckerman [17]. Finally, when Eq. (17), or their thermostatted analogs in Eq. (19) are integrated via an MTS algorithm, resonances are avoided [17]. The dynamics generated in Eq. (17) or Eq. (19) are referred to as *regulated dynamics* [17].

At this point, it is worth commenting on the role of the parameter L. If an average $\langle m_\alpha v_\alpha^2\rangle$ over the canonical distribution of Eq. (16) is performed, the result is $Lk_\mathrm{B}T/(L+1)$, which becomes the true canonical average only when $L \to \infty$. This means that MTS integration of Eq. (17) coupled to a thermostat in the limit that $L \to \infty$ would result in the very same resonances we are trying to avoid. In fact, since

$$L\ln\cosh\left(\frac{x}{\sqrt{L}}\right)=\frac{x^2}{2}-\frac{x^4}{12L}+\frac{x^6}{45L^2}\cdots \tag{20}$$

in the limit $L\to\infty$, Eq. (16) becomes the standard Hamiltonian of classical mechanics, for which there is no restriction on v_α. Thus, it is important to keep L finite and small. On the other hand, setting $L=1$ rather than, for instance, $L=4$, can disfavor diffusivity [17] and lead to somewhat larger correlation times [31]. As was shown by Abreu and Tuckerman [17], optimal resonance avoidance is generally obtained for $1<L\leq 4$, which largely agrees with optimal values of L in the isokinetic scheme [13,31].

Due to its simplicity, regulated dynamics is readily extendable to isobaric ensembles. Caution is necessary, however, due to the effect of MTS integration on the internal pressure of molecular systems. It has been observed that the usual atomic pressure can become a poor estimator when intra- and intermolecular interactions are split apart into fast and slow force components, respectively [3,33,34]. This can cause distortions in the mean bond lengths and angles which are too small to affect the potentially energy substantially, but can nevertheless impair the atomic virial. For this reason, it is better to rely on the molecular pressure when implementing a barostat algorithm [21,35,36].

We now introduce a formulation for constant-pressure simulations within the regulated dynamics approach. It is a version of the Martyna–Tobias–Klein (MTK) algorithm [37] with isotropic scaling of molecular centers of mass (instead of individual atomic coordinates) [21] applied to a system whose Hamiltonian is given by Eq. (16). In the case of a three-dimensional system whose N atoms are distributed among n molecules, the total mass, the center of mass, and the total momentum of a molecule j are, respectively,

$$M_j=\sum_{i\in j}m_i,\qquad \mathbf{R}_j=\frac{1}{M_j}\sum_{i\in j}m_i\mathbf{r}_i,\qquad \mathbf{P}_j=\sum_{i\in j}\mathbf{p}_i, \tag{21}$$

where $\sum_{i\in j}$ is a sum over every atom i in a molecule j. The center-of-mass velocity of such molecule is defined as

$$\mathbf{V}_j=\frac{1}{M_j}\sum_{i\in j}m_i\mathbf{v}_i, \tag{22}$$

where $\mathbf{v}_i$ is the velocity of atom i, whose component in the α direction ($\alpha=x,y,z$) is given by

$$v_{i\alpha}=c_i\tanh\left(\frac{p_{i\alpha}}{m_ic_i}\right). \tag{23}$$

Note that the usual relation between vectors $\mathbf{v}_i$ and $\mathbf{p}_i$ (which makes them parallel) no longer holds and, therefore, nor does it hold between $\mathbf{V}_j$ and $\mathbf{P}_j$. For a given external pressure P, we can sample an isoenthalpic–isobaric ensemble by means of the following equations of motion for atoms $i=1,\ldots,N$:

$$\begin{aligned}
\dot{\mathbf{r}}_i&=\mathbf{v}_i+\frac{p_\epsilon}{W}\mathbf{R}_{\mu_i}\\
\dot{\mathbf{p}}_i&=\mathbf{F}_i-\frac{n+1}{n}\frac{p_\epsilon}{W}\frac{m_i}{M_{\mu_i}}\mathbf{P}_{\mu_i}\\
\dot{V}&=3V\frac{p_\epsilon}{W}\\
\dot{p}_\epsilon&=3V(\mathcal{P}_{\mathrm{mol}}-P)+\frac{1}{n}\sum_{j=1}^{n}\mathbf{P}_j\cdot\mathbf{V}_j,
\end{aligned} \tag{24}$$

where μ_i is the index of the molecule that contains atom i, V is the system volume (which becomes a dynamical variable in isobaric molecular dynamics approaches), p_ϵ is the momentum of a redundant variable ϵ for which $\dot{V}=3V\dot{\epsilon}$, and W is a piston mass-like parameter. The internal molecular pressure $\mathcal{P}_{\mathrm{mol}}$ is defined as

$$\mathcal{P}_{\mathrm{mol}}=\frac{1}{3V}\sum_{j=1}^{n}(\mathbf{P}_j\cdot\mathbf{V}_j+\mathbf{R}_j\cdot\boldsymbol{\mathcal{F}}_j)-\frac{\partial U}{\partial V}, \tag{25}$$

where $\boldsymbol{\mathcal{F}}_j=\sum_{i\in j}\mathbf{F}_i$ is the resultant force exerted on molecule j, and we allow for a possible explicit dependence of the potential energy with volume. Because intramolecular forces cancel out in the computation of $\boldsymbol{\mathcal{F}}_j$, they do not contribute to $\mathcal{P}_{\mathrm{mol}}$. Eq. (24) conserve the energy function $H=\mathcal{H}(\mathbf{r},\mathbf{p})+PV+p_\epsilon^2/(2W)$, where $\mathcal{H}(\mathbf{r},\mathbf{p})$ is the Hamiltonian in Eq. (16).

For isothermal–isobaric sampling, we can make an individual thermostat act on every degree of freedom, including the extra momentum p_ϵ associated with the volume fluctuations. Nosé–Hoover chains [14] as well as Nosé–Hoover–Langevin thermostats [15,16] are suited for this task. Here we employ the latter, which consists in solving, for all $i=1,\ldots,N$ and $\alpha=x,y,z$, the stochastic differential equation system

$$\begin{aligned}
\mathrm{d}\mathbf{r}_i&=\left(\mathbf{v}_i+\frac{p_\epsilon}{W}\mathbf{R}_{\mu_i}\right)\mathrm{d}t\\
\mathrm{d}\mathbf{p}_i&=\left(\mathbf{F}_i-\mathbf{u}_i\circ\mathbf{p}_i-\frac{n+1}{n}\frac{p_\epsilon}{W}\frac{m_i}{M_{\mu_i}}\mathbf{P}_{\mu_i}\right)\mathrm{d}t\\
\mathrm{d}V&=3V\frac{p_\epsilon}{W}\mathrm{d}t\\
\mathrm{d}p_\epsilon&=\left[3V(\mathcal{P}_{\mathrm{mol}}-P)+\frac{1}{n}\sum_{j=1}^{n}\mathbf{P}_j\cdot\mathbf{V}_j-u_\epsilon p_\epsilon\right]\mathrm{d}t\\
\mathrm{d}u_{i\alpha}&=\frac{p_{i\alpha}v_{i\alpha}-k_{\mathrm{B}}T}{\mathcal{Q}_{i\alpha}}\mathrm{d}t-\gamma_{i\alpha}u_{i\alpha}\mathrm{d}t+\sigma_{i\alpha}\mathrm{d}w_{i\alpha}\\
\mathrm{d}u_\epsilon&=\frac{p_\epsilon^2/W-k_{\mathrm{B}}T}{\mathcal{Q}_\epsilon}\mathrm{d}t-\gamma_\epsilon u_\epsilon\mathrm{d}t+\sigma_\epsilon\mathrm{d}w_\epsilon,
\end{aligned} \tag{26}$$

where $\circ$ denotes an entrywise (Hadamard) product, and the $\mathcal{Q}$, γ, and σ parameters are the analogues of those in Eqs. (14) and (19).

We now describe a MTS integration algorithm for Eq. (26), which we have implemented in the LAMMPS software package [38,39]. Two of its particular features deserve special attention. First, although $\mathcal{P}_{\mathrm{mol}}$

can depend on intermolecular forces that act on multiple timescales, pressure-driven translations of the barostat momentum p_ϵ are not split into such scales. This differs from what has been done in previous methods [33]. Instead, it takes place exclusively at the outermost recursion level. This is how LAMMPS currently handles other isobaric MTS integrators. Since the inertial parameter W is usually very large, the barostat dynamics is expected to respond almost adiabatically to the intermolecular forces, whose fast fluctuations are averaged out. Second, the thermostat variables and their influence on the particle and barostat momenta are integrated in the innermost recursion level (that is, the fastest timescale) using a middle-type scheme [40,41].

For the sake of clarity, we focus on a double timescale version of the algorithm, but extension to the general MTS case is straightforward. The RESPA factorization goes as

$$e^{\Delta t\mathcal{L}} = e^{\frac{\Delta t}{2}\mathcal{L}^{\mathrm{tr}}_{p_\epsilon}} e^{\frac{\Delta t}{2}\mathcal{L}^{\mathrm{tr,s}}_{p}} \left[e^{\delta t\mathcal{L}_{\mathrm{ref}}}\right]^{n_{\mathrm{ref}}} e^{\frac{\Delta t}{2}\mathcal{L}^{\mathrm{tr,s}}_{p}} e^{\frac{\Delta t}{2}\mathcal{L}^{\mathrm{tr}}_{p_\epsilon}} \quad (27)$$

where 'tr' means translation and 's' refers to the slow force components. The Liouville operators involved in the slowest timescales are

$$\mathcal{L}^{\mathrm{tr}}_{p_\epsilon} = \left[3V(\mathcal{P}_{\mathrm{mol}} - P) + \frac{1}{n}\sum_{j=1}^{n}\mathbf{P}_j\cdot\mathbf{V}_j\right]\frac{\partial}{\partial p_\epsilon}$$
$$\mathcal{L}^{\mathrm{tr,s}}_{p} = \mathbf{F}_{\mathrm{s}}\cdot\frac{\partial}{\partial\mathbf{p}}. \quad (28)$$

The reference-system propagator is further split as

$$e^{\delta t\mathcal{L}_{\mathrm{ref}}} = e^{\frac{\delta t}{2}\mathcal{L}^{\mathrm{tr,f}}_{p}} e^{\frac{\delta t}{2}\mathcal{L}^{\mathrm{sc}}_{V}} e^{\frac{\delta t}{2}\mathcal{L}^{\mathrm{tr}}_{r}} e^{\delta t\mathcal{L}_{\mathrm{therm}}} e^{\frac{\delta t}{2}\mathcal{L}^{\mathrm{tr}}_{r}} e^{\frac{\delta t}{2}\mathcal{L}^{\mathrm{sc}}_{V}} e^{\frac{\delta t}{2}\mathcal{L}^{\mathrm{tr,f}}_{p}}, \quad (29)$$

where 'sc' stands for scaling and 'f' denotes the fast force components. The propagator $\exp(\delta t\mathcal{L}_{\mathrm{therm}})$, which lies in the middle of the factorization scheme, accounts for the thermostatting action. The other Liouville operators involved are

$$\mathcal{L}^{\mathrm{tr,f}}_{p} = \mathbf{F}_{\mathrm{f}}\cdot\frac{\partial}{\partial\mathbf{p}}$$
$$\mathcal{L}^{\mathrm{sc}}_{V} = \frac{p_\epsilon}{W}\left[3V\frac{\partial}{\partial V} + \sum_{i=1}^{N}\left(\mathbf{R}_{\mu_i}\cdot\frac{\partial}{\partial\mathbf{r}_i} - \frac{n+1}{n}\frac{m_i}{M_{\mu_i}}\mathbf{P}_{\mu_i}\cdot\frac{\partial}{\partial\mathbf{p}_i}\right)\right]$$
$$\mathcal{L}^{\mathrm{tr}}_{r} = \mathbf{v}\cdot\frac{\partial}{\partial\mathbf{r}}. \quad (30)$$

It is worth mentioning that the equations $\dot{V} = \mathcal{L}^{\mathrm{sc}}_V V$ and $\dot{\mathbf{r}} = \mathcal{L}^{\mathrm{sc}}_V\mathbf{r}$ result in a concerted scaling of the volume and all molecular center-of-mass coordinates, while the displacement of each atom i from the center of its containing molecule, $\mathbf{r}_i - \mathbf{R}_{\mu_i}$, remains constant. Simultaneously, $\dot{\mathbf{p}} = \mathcal{L}^{\mathrm{sc}}_V\mathbf{p}$ results in a scaling of all molecular center-of-mass momenta, while the difference $\mathbf{p}_i/m_i - \mathbf{P}_{\mu_i}/M_{\mu_i}$ also remains constant for every atom i.

Finally, the Nosé–Hoover–Langevin thermostats and their effects on the atom and barostat momenta are integrated as follows: [42]:

$$e^{\delta t\mathcal{L}_{\mathrm{therm}}} = e^{\frac{\delta t}{2}\mathcal{L}^{\mathrm{tr}}_{u}} e^{\frac{\delta t}{2}\mathcal{L}^{\mathrm{sc}}_{p}} e^{\delta t\mathcal{L}^{\mathrm{ou}}_{u}} e^{\frac{\delta t}{2}\mathcal{L}^{\mathrm{sc}}_{p}} e^{\frac{\delta t}{2}\mathcal{L}^{\mathrm{tr}}_{u}}, \quad (31)$$

where

$$\mathcal{L}^{\mathrm{tr}}_{u} = \frac{p_\epsilon^2/W - k_{\mathrm{B}}T}{\mathcal{Q}_\epsilon}\frac{\partial}{\partial u_\epsilon} + \sum_{i=1}^{N}\sum_{\alpha=x}^{z}\frac{p_{i\alpha}v_{i\alpha} - k_{\mathrm{B}}T}{\mathcal{Q}_{i\alpha}}\frac{\partial}{\partial u_{i\alpha}}$$
$$\mathcal{L}^{\mathrm{sc}}_{p} = -u_\epsilon p_\epsilon\frac{\partial}{\partial p_\epsilon} - \sum_{i=1}^{N}\sum_{\alpha=x}^{z}u_{i\alpha}p_{i\alpha}\frac{\partial}{\partial p_{i\alpha}} \quad (32)$$

and $\exp(\delta t\mathcal{L}^{\mathrm{ou}}_u)$ represents $3N+1$ independent Ornstein–Uhlenbeck processes involving u_ϵ and all $u_{i\alpha}$.

4 Results

In what follows, we present new results obtained from multiple timescale simulations of liquid-phase systems carried out in cubic boxes with periodic boundary conditions. By means of a 5th-degree smoothstep function [43], Lennard–Jones interactions are gradually switched to zero from $r = r_s = 11$ Å up to $r = r_c = 12$ Å. Lattice-sum methods [44,45] are employed for electrostatic interaction with the same cutoff distance r_c applied for the real-space contribution. Multiple time-stepping is done by splitting the forces into two timescales if $\Delta t \leq 3$ fs or three timescales if testing for stability and accuracy when very large outer time steps are employed. In either case, harmonic bond stretching and angle bending are allocated to the smallest timescale and integrated with an inner time step size $\delta t_{\mathrm{fast}} = 0.5$ fs. When $\Delta t \leq 3$ fs, the slowest terms are the ones due to the full Lennard–Jones and electrostatic interactions. Otherwise, these non-bonded forces are split into two (middle and outer) timescales by means of the RESPA2 scheme [13,46,47]. In the middle timescale, every pair force (rather than the corresponding pair potential) gradually decays to zero from $r = r_s^{\mathrm{in}} = 5$ Å up to $r = r_c^{\mathrm{in}} = 8$ Å, once again using a 5th-degree smoothstep function [43]. The integration time step in this middle scale is $\delta t_{\mathrm{middle}} = 3$ fs. In a complementary manner, these forces change from zero to their full values in the outer timescale, whose integration is done at different values of $\delta t_{\mathrm{slow}} = \Delta t$, thus allowing us to evaluate how large this time step can be made without affecting observable properties. The mass-like parameters and friction coefficients of the stochastic thermostats have the same values for all atomic degrees of freedom and are computed from a specified characteristic time $\tau_p = 20\delta t_{\mathrm{fast}} = 10$ fs, respectively as $\mathcal{Q}_{i\alpha} = k_{\mathrm{B}}T\tau_p^2$ and $\gamma_{i\alpha} = \tau_p^{-1}$.

Our first example is the calculation of a solvation free energy in the canonical ensemble. Solvation free energy is an important property whose calculation via molecular dynamics can be accelerated by the use of multiple time-stepping. In a previous study [31], we

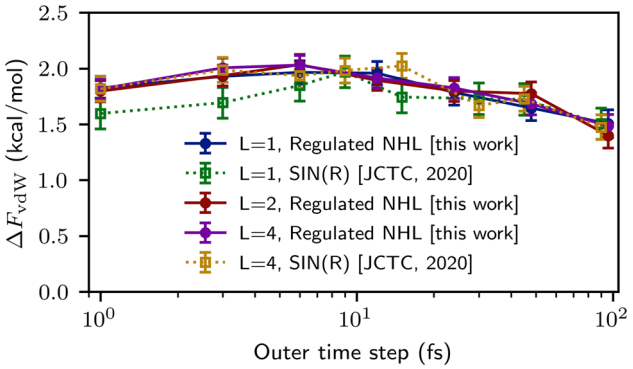

Fig. 1 Contribution of van der Waals interactions to the hydration free energy of phenol. The solute and solvent were modeled using the GAFF [48] and SPC-Fw [49] force fields, respectively. The SIN(R) results are those recently published in Ref. [31]

employed the SIN(R) method to compute hydration free energies of organic molecules using values up to 90 fs for the outer time step without observing resonance artifacts. In Fig. 1, we show that the same performance is attainable with the simpler, regulated-dynamics version of the Nosé–Hoover–Langevin algorithms presented in Eq. (19). For this example, we simulated the alchemical coupling/decoupling of a single phenol molecule in a box with constant $V = 14.728$ nm^3 and $T = 298.15$ K containing 499 water molecules, totaling $n = 500$. The modeling was done using GAFF [48] parameters for phenol and the SPC-Fw [49] parameters for water. Standard long-range corrections [21] were applied for the Lennard–Jones interactions, and the smooth particle-mesh Ewald (SPME) method [45] was used for computing electrostatic interactions. The force splitting strategy, as well as the integration method, were implemented using OpenMM's customization features [50].

Figure 1 shows the van der Waals contribution to the coupling free energy, obtained by applying a softcore potential [51] to the solute–solvent interactions. This potential depends on a coupling parameter λ in such a way that the Lennard–Jones potential is fully recovered when $\lambda = 1$ and completely vanishes when $\lambda = 0$. Note that the van der Waals contribution is the most challenging to generate. For each combination of regulation parameter L and time-step size Δt, we performed 21 simulations with different λ values evenly spaced from 0 to 1. Although L can assume non-integer values, the ones we selected for our tests were 1, 2, and 4, aiming at a direct comparison with previous results obtained with the SIN(R) method [31]. The total time of each simulation was 9.6 ns. During the last 80% of this time and at regular intervals of 960 fs, we computed and stored softcore energies at the λ state in question and at the 20 additional states as well. The combined sample resulting from the 21 simulations was then post-processed according to the Multistate Bennett Acceptance Ratio (MBAR) method [52], thus producing a point for Fig. 1 and its corresponding error bar. The combination of regulation parameters equal to 1, 2, and 4 with outer time-step sizes equal to 1, 3, 6, 12, 24, 48, and 96 fs resulted in ~ 4.2 μs of simulated time and allowed us to build the three solid curves of Fig. 1. The figure also contains dotted curves reproducing the previously published results for the same system using isokinetic constraints instead of regulated dynamics as a means of avoiding resonances [31]. The isokinetic runs were performed at different values of outer time steps, specifically, 1, 3, 6, 9, 15, 30, 45, and 90 fs for shorter simulation times (4.5 ns each). The comparison shows that both methodologies are similarly effective, with a variation over the entire range of outer time steps of no more than a few tenths of a kcal/mol.

We now present results from isothermal–isobaric (i.e. constant-NPT) simulations carried out with our newly developed regulated dynamics method described in Eq. (26). We have implemented the method in the LAMMPS software package [38,39]. The system studied is bulk liquid water using the SPC-Fw model [49]. The system consists of $n = 700$ molecules, and the simulations are carried out at $T = 300$ K and $P = 1$ atm. All Lennard–Jones interactions, including tail corrections, were neglected beyond the cutoff distance r_c. For electrostatic interactions, we employed the PPPM Ewald method [44] with parameters and grid spacing adjusted to yield a relative accuracy of about 10^{-7} in the force computations. In addition to the thermostats coupled to the atomic degrees of freedom, we also employ a Nosé–Hoover–Langevin thermostat to control the temperature of the barostat variable. The mass-like parameter and friction coefficient of this additional thermostat are determined using the formulae $\mathcal{Q}_\epsilon = (3n+1)k_{\rm B}T\tau_b^2$ and $\gamma_\epsilon = \tau_b^{-1}$, respectively, where τ_b is a characteristic time associated with volume fluctuations. In our simulations, we employed $\tau_b = 200\delta t_{\rm fast} = 100$ fs. Each simulation consisted of 1.2 ns of equilibration, followed by 4.8 ns of production, with property sampling every 96 fs. Results for average properties are shown in Fig. 2. Specifically, we show the average potential energy per molecule, the molar volume, and the molecular and atomic pressure estimators across the range of time steps for different values of the regulation parameter L. For regulated dynamics, the atomic pressure estimator is given by

$$\mathcal{P}_{\rm atom} = \frac{1}{3V}\sum_{i=1}^{N}(\mathbf{p}_i\cdot\mathbf{v}_i + \mathbf{r}_i\cdot\mathbf{F}_i) - \frac{\partial U}{\partial V}. \qquad (33)$$

The error bars on the molecular pressure estimator panel represent 95% confidence intervals obtained from correlation times estimated by an integrated autocorrelation function method [53]. The horizontal lines in the panels showing the potential energy per molecule and molar volume are results from a single time-step run using the NHL thermostat with a 0.5 fs time step (10 ns of production after 2 ns of equilibration). In the panels showing the molecular and atomic pressure estimators, the horizontal line is placed at 1 atm, which is the value specified for the external applied pressure.

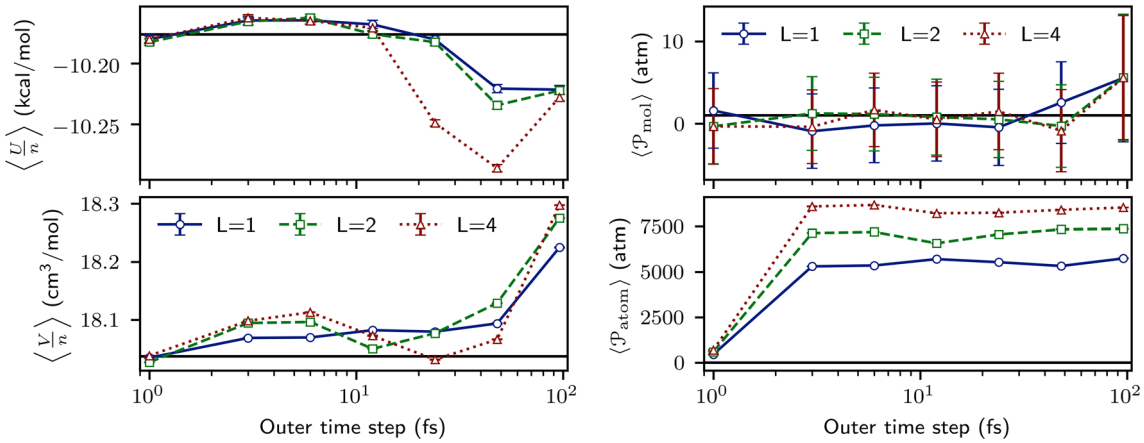

Fig. 2 Isothermal–isobaric simulation results for SPC-Fw water at $T = 300$ K and $P = 1$ atm

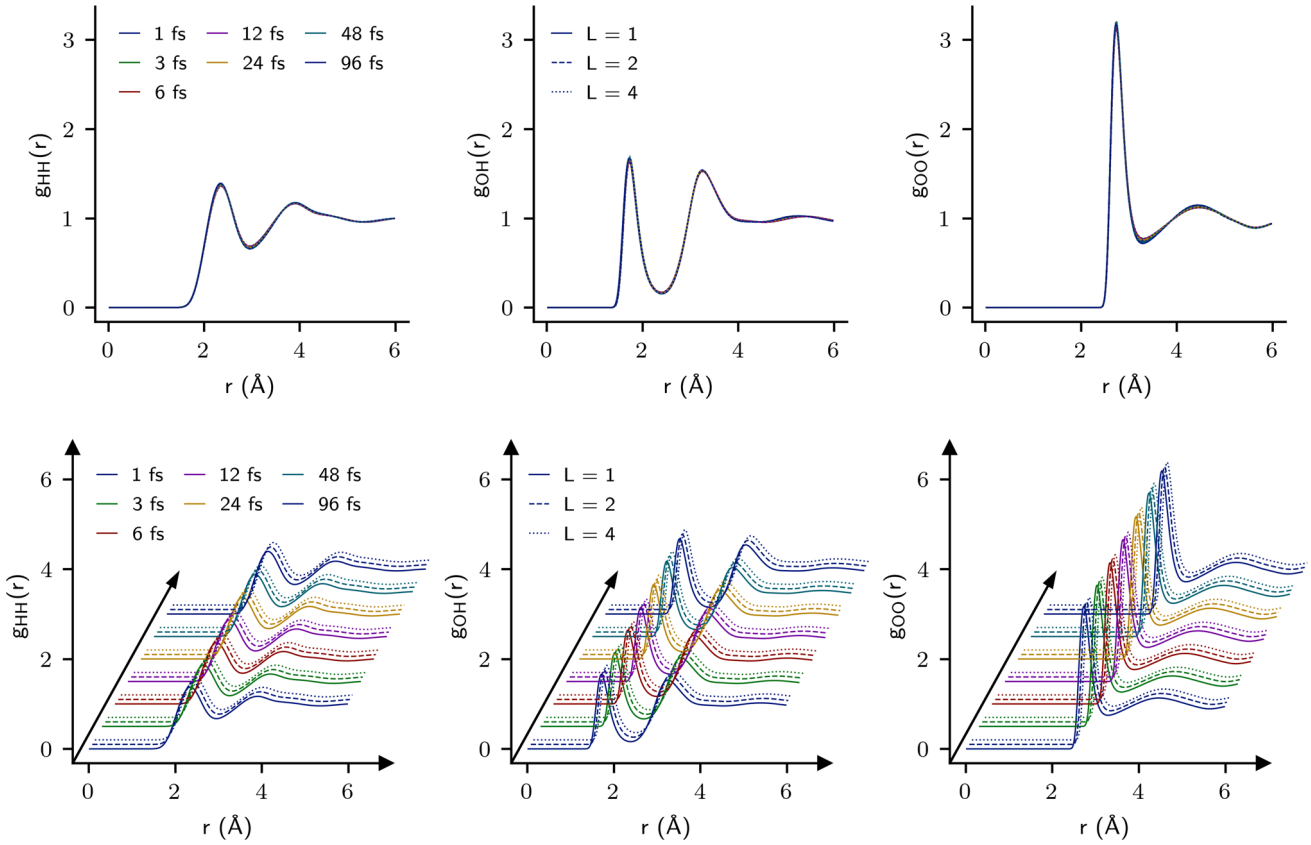

Fig. 3 Intermolecular radial distribution functions obtained from isothermal–isobaric simulations of 700 SPC-Fw [49] water molecules (under periodic boundary conditions) at $T = 300$ K and $P = 1$ atm

Figure 2 shows that even at the largest time steps, the molar volume changes by no more than a few percent, and the average potential energy per molecule changes by only a few hundredths of a kcal/mol. Molecular pressures change by a few atmospheres but still lie within the error bars of each other across the full range of time steps. Note, however, as alluded to earlier, changes in the atomic pressure estimator are significantly more dramatic as a function of outer time step.

To assess how the sensitivities in the quantities shown in Fig. 2 affect an actual observable, we show the water radial distribution functions (RDFs), $g_{\mathrm{OO}}(r)$, $g_{\mathrm{OH}}(r)$, and $g_{\mathrm{HH}}(r)$ for different values of L across the range of time steps shown in Fig. 3. The top three panels show that all RDFs are nearly indistinguishable from each other. The bottom three panels show the various distributions in a manner that is easier to distinguish the results at different time steps and different values of L, and it is clear that there is only negligible variation

Table 1 Isothermal–isobaric simulation speeds of the regulated NHL method with various outer time-step size (Δt) and regulation parameter (L) values, as well as that of the standard NHL method with $\Delta t = 0.5$ fs. The same code and parallelization protocol were applied for all simulations, executed in multiple nodes of a uniform computer cluster

Δt (fs)	Execution speed (ns/day)		
0.5	3.05		
	(L=1)	(L=2)	(L=4)
1	6.12	5.83	5.50
3	13.7	15.0	15.7
6	25.5	24.2	25.9
12	36.9	33.4	36.8
24	40.9	48.6	46.5
48	55.9	56.5	55.4
96	60.8	62.2	61.4

in these distribution functions across all time steps and L values employed.

It is worth noting that in our LAMMPS implementation, the savings in computational time when a 96 fs outer time step is employed is roughly a factor of 20 over a single time-step benchmark run with a time step of 0.5 fs. This factor is essentially unchanged over all values of L, as reported in Table 1.

5 Avoiding resonances using a colored-noise Langevin equation

Recently, generalized Langevin equations (GLEs) have been employed to create bath models for MD simulations [54] that accomplish a variety of tasks including mimicking quantum effects [55,56], reducing the bead number in path-integral calculations [57,58], and staving off the resonances that plague MTS methods [9]. In this section, we will conclude our discussion of MTS methodology by providing a brief review of the general framework for "designer" memory kernels [54] and then showing how a kernel capable of mollifying resonances in multiple time-step MD can be designed.

The generalized Langevin equation for a coordinate r_α and momentum p_α with associated mass m_α can be written as

$$\begin{aligned} \mathrm{d}r_\alpha &= \frac{p_\alpha}{m_\alpha}\mathrm{d}t \\ \mathrm{d}p_\alpha &= F_\alpha(\mathbf{r})\mathrm{d}t \\ &\quad - \left[\int_0^t \mathrm{d}\,\tau\, p_\alpha(\tau)K(t-\tau)\right]\mathrm{d}t + \sigma_\alpha \mathrm{d}w_\alpha, \end{aligned} \tag{34}$$

for $t \geq 0$. In this section, we will assume the memory kernel $K(t)$ is a combination of exponential and δ-function forms

$$K(t) = \zeta_0\delta(t) - \tilde{\boldsymbol{\gamma}}^{\mathsf{T}} e^{-|t|\boldsymbol{\Gamma}}\boldsymbol{\gamma} \tag{35}$$

which is defined for $t \in (-\infty, \infty)$. Here ζ_0 is a constant, $\boldsymbol{\gamma}$ is a column vector having ν components, $\tilde{\boldsymbol{\gamma}}^{\mathsf{T}}$ is an ν-component row vector, and $\boldsymbol{\Gamma}$ is an $\nu \times \nu$ matrix. By adding more exponential terms, the parameter ν adds flexibility to the design of memory kernels given Eq. (35). For this particular form of the friction kernel, the GLE can be written in the form of a standard Langevin equation in an extended phase space with ν additional variables $s_1, ..., s_\nu \equiv \mathbf{s}$. This extended phase-space formulation of the Langevin equation takes the form

$$\begin{aligned} \mathrm{d}r_\alpha &= \frac{p_\alpha}{m_\alpha}\mathrm{d}t \\ \mathrm{d}\begin{pmatrix} p_\alpha \\ \mathbf{s} \end{pmatrix} &= \begin{pmatrix} F_\alpha(\mathbf{r}) \\ \mathbf{0} \end{pmatrix}\mathrm{d}t - \mathbf{Z}\begin{pmatrix} p_\alpha \\ \mathbf{s} \end{pmatrix}\mathrm{d}t + \mathbf{B}_\alpha \mathrm{d}\boldsymbol{\xi}_\alpha, \end{aligned} \tag{36}$$

where $\mathrm{d}\boldsymbol{\xi}_\alpha(t)$ is a vector of infinitesimal Wiener processes, $\mathbf{Z}$ is a $(\nu+1)\times(\nu+1)$ matrix

$$\mathbf{Z} = \begin{pmatrix} \zeta_0 & \tilde{\boldsymbol{\gamma}}^{\mathsf{T}} \\ \boldsymbol{\gamma} & \boldsymbol{\Gamma} \end{pmatrix} \tag{37}$$

known as the damping matrix or drift matrix, and $\mathbf{B}_\alpha$ is a $(\nu+1)\times(\nu+1)$ diffusion matrix. The equivalence between Eq. (36) and (34) with memory kernel given by Eq. (35) can be seen by solving Eq. (36) for $\mathbf{s}(t)$ in terms of $p_\alpha(t)$ and then substituting the result into Eq. (34). The second fluctuation dissipation theorem allows us to derive a relation between the matrices $\mathbf{B}$ and $\boldsymbol{\zeta}$. This connection takes the form of a matrix equation

$$m_\alpha kT\left(\mathbf{Z} + \mathbf{Z}^{\mathsf{T}}\right) = \mathbf{B}_\alpha^{\mathsf{T}}\mathbf{B}_\alpha. \tag{38}$$

Equation (38) implies that $\mathbf{Z}+\mathbf{Z}^{\mathsf{T}}$, which is the symmetric part of $\mathbf{Z}$, must be positive definite. Since Eq. (36) is an ordinary Langevin equation in the extended phase space, it can be integrated using the Matthews–Leimkuhler algorithm [59]. Nevertheless, it encodes the memory of Eq. (35), which can be chosen *a priori* to model a colored-noise bath with features that influence a simulation in a desired manner. In other words, Eq. (36) allows us to design memory kernels for performing specific types of simulations while retaining the simplicity of the Langevin equation.

Because the elements of $\mathbf{Z}$ are contained in the general exponential memory kernel of Eq. (35), designing a kernel for a specific task is tantamount to customizing the drift matrix $\mathbf{Z}$. Based on the framework presented, we can glean several important restrictions on possible choices of $\mathbf{Z}$. From Eq. (35), it is clear that the Z_{11} element is simply the white-noise term and that the time dependence, hence the memory component, is encoded in the matrix $\boldsymbol{\Gamma}$. Given this, it is important to note that Eq. (36) will only be able to recover an equilibrium ensemble as $t \to \infty$ provided $K(t)$ has a finite

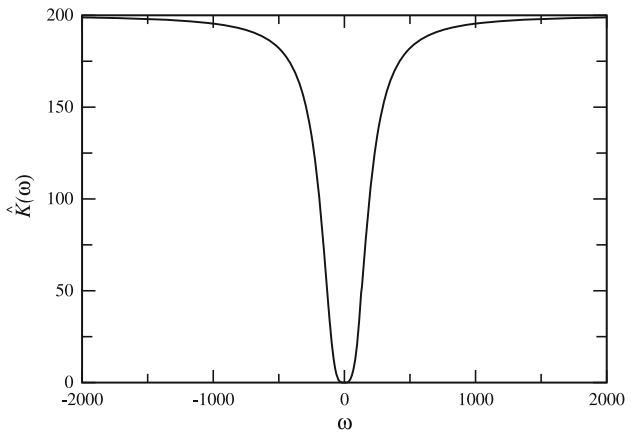

Fig. 4 Desired behavior of the Fourier transform of the memory kernel

decay time, and this, therefore, requires that the real part of the eigenvalues of $\mathbf{\Gamma}$ be positive. Choosing drift matrices that satisfy requirements such as these can be nontrivial, and each choice should be carefully tested for its compliance with the requirements and its ability to produce stable dynamics.

With these caveats in mind, let us consider how we might design a kernel to mollify resonance behavior in MTS MD simulations. Recall that resonances occur from the influence of high-frequency motion, integrated using the smallest (inner) time steps, on intermediate and long timescales, integrated using larger (outer) time steps. Thus, the key feature that a bath model should have is strong coupling to the highest frequencies, leading to strong damping of these frequencies, and weaker coupling or small perturbation of lower frequencies. These considerations suggest that our starting point should be to identify the frequency dependence of the memory kernel, *i.e.*, we should start with the Fourier transform of $K(t)$:

$$\hat{K}(\omega) = \frac{1}{\sqrt{2\pi}} \int_{-\infty}^{\infty} K(t) e^{-i\omega t}\, \mathrm{d}t. \tag{39}$$

Based on the desire for the friction to couple strongly to high frequencies and weakly to low frequencies, we can intuit what the general shape of $\hat{K}(\omega)$ should be, and we show this general behavior illustratively in Fig. 4.

Since $\hat{K}(\omega)$ determines the strength of the coupling at a given value of ω, it can be seen that at the extremes, where $|\omega|$ is large, $\hat{K}(\omega)$ is large as well, while near $\omega \approx 0$, $\hat{K}(\omega) \approx 0$. While there are many functional forms that could, in principle, produce the behavior in Fig. 4, we need a functional form that is consistent with a Fourier transform of Eq. (35), and since Eq. (35) is a sum of simple exponentials, $\hat{K}(\omega)$ should be composed of Lorentzian functions. For example, consider $\hat{K}(\omega)$ in the form

$$\hat{K}(\omega) = \sqrt{2\pi}\zeta_0 - \frac{\zeta_0}{2}\left[\frac{\tilde{\omega}^2}{\frac{3}{4}\tilde{\omega}^2 + \left(\omega - \frac{\tilde{\omega}}{2}\right)^2} + \frac{\tilde{\omega}^2}{\frac{3}{4}\tilde{\omega}^2 + \left(\omega + \frac{\tilde{\omega}}{2}\right)^2}\right]. \tag{40}$$

This kernel is a sum of two Lorentzian functions centered at $\omega = \pm\tilde{\omega}/2$ subtracted from a constant $\sqrt{2\pi}\zeta_0$. The corresponding memory kernel $K(t)$ is

$$K(t) = \zeta_0\delta(t) - \sqrt{\frac{2\pi}{3}}\tilde{\omega}\zeta_0 e^{-\sqrt{3}\tilde{\omega}|t|/2}\cos\left(\tilde{\omega}t/2\right). \tag{41}$$

Given the fact that $K(t)$ contains two exponentials (which becomes clear when $\cos(\tilde{\omega}t/2)$ is written as $(\exp(i\tilde{\omega}t/2) + \exp(-i\tilde{\omega}t/2))/2$), we then need $\nu = 2$ extended variables s_1 and s_2, which means that the drift matrix Γ is a 3×3 matrix. The 2×2 submatrix $\mathbf{\Gamma}$ must have eigenvalues $(\tilde{\omega}\sqrt{3}/2) \pm (i\tilde{\omega}/2)$, and a 2×2 matrix that gives us these is

$$\mathbf{\Gamma} = \begin{pmatrix} \tilde{\omega}\sqrt{3} & \tilde{\omega} \\ -\tilde{\omega} & 0 \end{pmatrix}. \tag{42}$$

The vectors $\tilde{\boldsymbol{\gamma}}^{\mathsf{T}}$ and $\boldsymbol{\gamma}$ have components proportional to $(\zeta_0\tilde{\omega})^{1/2}$, i.e., $\tilde{\boldsymbol{\gamma}}^{\mathsf{T}} = (\zeta_0\tilde{\omega})^{1/2}(a \quad b)$ and $\boldsymbol{\gamma}^{\mathsf{T}} = (\zeta_0\tilde{\omega})^{1/2}(a \quad -b)$, where a and b are simple numerical constants.

In Ref. [9], the authors considered a flexible model of water [60], for which the colored-noise Langevin scheme is used to compute the diffusion constant using a three time-step multiple time-stepping scheme. Since diffusion is dominated by low-frequency motion, the strong coupling between high-frequency modes to the bath should allow a large outer time step without affecting the diffusion constant. In this scheme, a time step of 0.5 fs is used for bonded interactions, non-bonded interactions within 9 Å are integrated with a 2 fs time step, and the outer time step is varied. The correct diffusion constant for the model is 0.25 Å^2/ps. When the colored noise scheme is used with outer time steps of 12 fs, 16 fs, and 20 fs, the resulting diffusion constants are 0.24 Å^2/ps, 0.20 Å^2/ps, and 0.16 Å^2/ps, respectively [9]. By contrast, when a simple white-noise Langevin scheme is used with a friction value of 1 ps^{-1}, the resulting diffusion constants for outer time steps of 12 fs, 16 fs, and 20 fs are 0.095 Å^2/ps, 0.044 Å^2/ps, and 0.019 Å^2/ps, respectively. This example illustrates how effective the colored-noise method is at mollifying resonances, allowing an outer time step of 12 fs to be achieved with minimal perturbation to the rate of diffusion, showing that it is possible, within the colored-noise framework, to preserve certain dynamical properties, specifically, those associated with the low-frequency modes of a system.

6 Discussion and conclusions

MTS algorithms have advanced through the decades from early attempts that failed to preserve time-reversibility [61–66] to reversible, symplectic algorithms [1–3] limited by resonance artifacts [4–6] and, ultimately, to the resonance-free methods discussed in this article that finally realize the large time steps that the force decompositions discussed here should allow [9,13,17,29,31,67]. MTS algorithms have been applied to increase the efficiency of path-integral simulations [23,68], *ab initio* molecular dynamics simulations in which the interatomic forces are computed "on the fly" from electronic structure calculations [68–71], to related polarizable force field calculations in which polarization forces are computed "on the fly" from charges and local dipoles [29,30,72], and to coarse-grained models [73].

Although the achievements of MTS algorithms are notable, significant challenges are on the horizon. The advent of machine learning potentials [74] brings new questions about how to decompose the forces derived from these non-physics-based forms into fast and slow components. Given the higher computational overhead associated with these machine learning potentials over conventional fixed-charge physics-based force fields, increasing the efficiency of simulations employing these potentials is highly desirable. One potential approach for developing MTS algorithms for machine learning potentials is to employ a computationally cheaper force field as the reference system and use the machine learning potential to derive a presumably slowly varying correction via $\mathbf{F}_{\mathrm{s}} = \mathbf{F}_{\mathrm{ML}} - \mathbf{F}_{\mathrm{ff}}$. This approach could be applied for both non-reactive and reactive systems. For neural network potentials, it may also be possible to identify rapidly and slowly varying subnetworks [75], thus allowing direct decomposition of forces. Machine learning techniques can also be leveraged to design MTS algorithms through analysis of the actual time series [76] or, perhaps, to parameterize memory kernels for improvement of the colored-noise (GLE) approach described in the previous section. In addition to paradigm-shifting machine learning models of physical interactions, advances in high-performance computing hardware also bring new challenges for MTS algorithms. Graphical processing units (GPUs) change the load balance and computational overhead associated with certain parts of a force calculation, e.g., nonbonded forces, compared to CPUs. Therefore, devising MTS algorithms that map well to GPUs [77] remains a key challenge.

The immediate future will likely see harvesting of low-hanging fruits such as extension of the isobaric regulated dynamics for anisotropic cell fluctuations, combining SIN(R) and regulated dynamics with aggressive thermostats such as the generalized Gaussian moment algorithm [78], and testing the Hamiltonian of regulated dynamics for its ability to describe dynamical properties without significantly compromising the time-step gains by means of the L parameter.

To conclude, we note that MTS algorithms have influenced essentially all flavors of MD simulations for the past three decades, and their universal nature and ubiquity of timescale separation in physical systems means that they will likely continue to do so going forward. In this article, we have reviewed the basic MTS approach and have shown how several creative schemes have greatly enhanced their performance. We have alluded to the new challenges that will confront MTS algorithms in the near future. We hope that the range of approaches described in this article gives a sense of the kind of thinking that will be needed to address these challenges for next-generation MTS methods.

Acknowledgements C.R.A.A. thanks the Federal University of Rio de Janeiro for a sabbatical leave and the New York University for a visiting scholar program membership. M.E.T. acknowledges funding from the National Science Foundation through grant no. CHE-1955381.

Author contributions

Both authors contributed equally to the conceptualization and writing of this manuscript.

Data Availability Statement The manuscript has associated data in a data repository. [Authors' comment: The data will be made available by making a request to either of the authors.]

References

1. H. Grubmüller, H. Heller, A. Windemuth, K. Schulten, Mol. Simul **6**(1–3), 121 (1991)
2. M. Tuckerman, B.J. Berne, G.J. Martyna, J. Chem. Phys. **97**(3), 1990 (1992). https://doi.org/10.1063/1.463137
3. G.J. Martyna, M.E. Tuckerman, D.J. Tobias, M.L. Klein, Mol. Phys. **87**(5), 1117 (1996)
4. J.J. Biesiadecki, R.D. Skeel, J. Comput. Phys. **109**(2), 318 (1993)
5. T. Schlick, M. Mandziuk, R.D. Skeel, K. Srinivas, J. Comput. Phys. **140**, 1 (1998)
6. Q. Ma, J.A. Izaguirre, R.D. Skeel, SIAM, J. Sci. Comput. **24**, 1951 (2003)
7. B. García-Archilla, J.M. Sanz-Serna, R.D. Skeel, SIAM J Sci. Comput. **20**(3), 930 (1998). https://doi.org/10.1137/s1064827596313851
8. R.D. Skeel, J.A. Izaguirre, in *Computational Molecular Dynamics: Challenges, Methods, Ideas*, vol. 4, ed. by M. Griebel, D.E. Keyes, R.M. Nieminen, D. Roose, T. Schlick, P. Deuflhard, J. Hermans, B. Leimkuhler, A.E. Mark, S. Reich, R.D. Skeel (Springer, Berlin Heidelberg, Berlin, Heidelberg, 1999), pp. 318–331
9. J.A. Morrone, T.E. Markland, M. Ceriotti, B.J. Berne, J. Chem. Phys. **134**(1), 014103 (2011)
10. P. Minary, G.J. Martyna, M.E. Tuckerman, J. Chem. Phys. **118**(6), 2510 (2003)

11. P. Minary, G.J. Martyna, M.E. Tuckerman, J. Chem. Phys. **118**(6), 2527 (2003)
12. P. Minary, M.E. Tuckerman, G.J. Martyna, Phys. Rev. Lett. **93**, 15 (2004)
13. B. Leimkuhler, D.T. Margul, M.E. Tuckerman, Mol. Phys. **111**(22–23), 3579 (2013)
14. G.J. Martyna, M.L. Klein, M. Tuckerman, J. Chem. Phys **97**(4), 2635 (1992)
15. A.A. Samoletov, C.P. Dettmann, M.A.J. Chaplain, J. Stat. Phys **128**(6), 1321 (2007)
16. B. Leimkuhler, E. Noorizadeh, F. Theil, J. Stat. Phys **135**(2), 261 (2009)
17. C.R.A. Abreu, M.E. Tuckerman, Molecular Physics p. e1923848 (2021). https://doi.org/10.1080/00268976.2021.1923848
18. S. Nosé, J. Chem. Phys. **81**(1), 511 (1984)
19. W.G. Hoover, Phys. Rev. A **31**(3), 1695 (1985)
20. R. Korol, N. Bou-Rabee, T.F. Miller, J. Chem. Phys. **151**(12), 124103 (2019)
21. M.E. Tuckerman, *Statistical mechanics: theory and molecular simulation* (Oxford University Press, Oxford, 2010)
22. M. Parrinello, A. Rahman, J. Chem. Phys. **80**, 860 (1984)
23. M.E. Tuckerman, G.J. Martyna, M.L. Klein, B.J. Berne, J. Chem. Phys. **99**, 2796 (1993)
24. S.J. Marrink, H.J. Risselada, S. Yefimov, D.P. Tieleman, A.H. de Vries, J. Phys. Chem. B **111**(27), 7812 (2007)
25. S. Kmiecik, D. Gront, M. Kolinski, L. Wieteska, A.E. Dawid, A. Kolinski, Chem. Rev. **116**(14), 7898 (2016)
26. A.E. Hafner, J. Krausser, A. Šarić, Curr. Opin. Struct. Biol. **58**, 43 (2019)
27. K. Kempfer, J. Devémy, A. Dequidt, M. Couty, P. Malfreyt, ACS Omega **4**(3), 5955 (2019)
28. E. Barth, T. Schlick, J. Chem. Phys. **109**, 1633 (1998)
29. D.T. Margul, M.E. Tuckerman, J. Chem. Theory Comput. **12**(5), 2170 (2016)
30. A. Albaugh, M.E. Tuckerman, T. Head-Gordon, J. Chem. Theory Comput. **15**(4), 2195 (2019)
31. C.R.A. Abreu, M.E. Tuckerman, J. Chem. Theory Comput. **16**(12), 7314 (2020)
32. K.F. Gauss, Reine Angew. Math. IV **232**(1829)
33. M.E. Tuckerman, J. Alejandre, R. Lopez-Rendon, A.L. Jochim, G.J. Martyna, J. Phys. A **39**(19), 5629 (2006). https://doi.org/10.1088/0305-4470/39/19/S18
34. Y. Andoh, N. Yoshii, A. Yamada, S. Okazaki, J. Comput. Chem. **38**(10), 704 (2017). https://doi.org/10.1002/jcc.24731
35. G. Kalibaeva, M. Ferrario, G. Ciccotti, Mol. Phys. **101**(6), 765 (2003). https://doi.org/10.1080/0026897021000044025
36. V. Marry, G. Ciccotti, J. Comput. Phys. **222**(1), 428 (2007). https://doi.org/10.1016/j.jcp.2006.07.033
37. G.J. Martyna, D.J. Tobias, M.L. Klein, J. Chem. Phys. **101**(5), 4177 (1994). https://doi.org/10.1063/1.467468
38. S. Plimpton, J.Comput.Phys. **117**(1), 1 (1995). https://doi.org/10.1006/jcph.1995.1039
39. S. Plimpton, A. Kohlmeyer, A. Thompson, S. Moore, R. Berger. Lammps stable release 29 october 2020 (2020). https://doi.org/10.5281/zenodo.3726416
40. Z. Zhang, X. Liu, Z. Chen, H. Zheng, K. Yan, J. Liu, J.Chem.Phys. **147**(3), 034109 (2017). https://doi.org/10.1063/1.4991621
41. Z. Zhang, X. Liu, K. Yan, M.E. Tuckerman, J. Liu, J. Phys. Chem. A **123**(28), 6056 (2019). https://doi.org/10.1021/acs.jpca.9b02771
42. B. Leimkuhler, C. Matthews, Molecular Dynamics With Deterministic and Stochastic Numerical Methods, Interdisciplinary Applied Mathematics, vol. 39 (Springer International Publishing, Cham, 2015). https://doi.org/10.1007/978-3-319-16375-8
43. T.S. Lee, Z. Lin, B.K. Allen, C. Lin, B.K. Radak, Y. Tao, H.C. Tsai, W. Sherman, D.M. York, J. Chem. Theory Comput. **16**(9), 5512 (2020). https://doi.org/10.1021/acs.jctc.0c00237
44. R.W. Hockney, J.W. Eastwood, *Computer simulation using particles* (Publisher, CRC Press, Boca Raton, 1988)
45. T. Darden, D. York, L. Pedersen, J. Chem. Phys. **98**(12), 10089 (1993)
46. R. Zhou, E. Harder, H. Xu, B.J. Berne, J. Chem. Phys. **115**(5), 2348 (2001). https://doi.org/10.1063/1.1385159
47. J.A. Morrone, R. Zhou, B.J. Berne, J. Chem. Theory Comput. **6**(6), 1798 (2010)
48. J. Wang, R.M. Wolf, J.W. Caldwell, P.A. Kollman, D.A. Case, J. Comput. Chem. **25**(9), 1157 (2004). https://doi.org/10.1002/jcc.20035
49. Y. Wu, H.L. Tepper, G.A. Voth, J. Chem. Phys. **124**(2), 024503 (2006). https://doi.org/10.1063/1.2136877
50. P. Eastman, J. Swails, J.D. Chodera, R.T. McGibbon, Y. Zhao, K.A. Beauchamp, L.P. Wang, A.C. Simmonett, M.P. Harrigan, C.D. Stern, R.P. Wiewiora, B.R. Brooks, V.S. Pande, PLOS Comput. Biol. **13**(7), e1005659 (2017)
51. T.C. Beutler, A.E. Mark, R.C. van Schaik, P.R. Gerber, W.F. van Gunsteren, Chem. Phys. Lett. **222**(6), 529 (1994). https://doi.org/10.1016/0009-2614(94)00397-1
52. M.R. Shirts, J.D. Chodera, J. Chem. Phys. **129**(12), 124105 (2008). https://doi.org/10.1063/1.2978177
53. J.D. Chodera, W.C. Swope, J.W. Pitera, C. Seok, K.A. Dill, J. Chem. Theory Comput. **3**(1), 26 (2007)
54. M. Ceriotti, G. Bussi, M. Parrinello, J Chem. Theory Comput. **6**(4), 1170 (2010)
55. M. Ceriotti, G. Bussi, M. Parrinello, Phys. Rev. Lett. **102**(2), 020601 (2009)
56. S. Ganeshan, R. Ramírez, M.V. Fernández-Serra, Phys. Rev. B **87**, 134207 (2013)
57. M. Ceriotti, M. Parrinello, T.E. Markland, D.E. Manolopoulos, J. Chem. Phys. **133**, 124104 (2010)
58. M. Ceriotti, D.E. Manolopoulos, M. Parrinello, J. Chem. Phys. **134**, 084104 (2011)
59. B. Leimkuhler, C. Matthews, Applied Mathematics Research eXpress (2012)
60. Y. Wu, H.L. Tepper, G.A. Voth, J. Chem. Phys. **124**, 024503 (2006)
61. R. Swindoll, J. Haile, J. Comput. Phys. **53**(2), 289 (1984)
62. O. Teleman, B. Jönsson, J. Comput. Chem. **7**(1), 58 (1986)
63. M.E. Tuckerman, G.J. Martyna, B.J. Berne, J. Chem. Phys. **93**(2), 1287 (1990)
64. M.E. Tuckerman, B.J. Berne, A. Rossi, J. Chem. Phys. **94**(2), 1465 (1991)
65. M.E. Tuckerman, B.J. Berne, G.J. Martyna, J. Chem. Phys. **94**(10), 6811 (1991)

66. M.E. Tuckerman, B.J. Berne, J. Chem. Phys. **95**(11), 8362 (1991)
67. P.Y. Chen, M.E. Tuckerman, J. Chem. Phys. **148**(2), 024106 (2018)
68. O. Marsalek, T.E. Markland, J. Chem. Phys. **144**(5), 054112 (2016)
69. N. Luehr, T.E. Markland, T.J. Martínez, J. Chem. Phys. **140**(8), 084116 (2014)
70. R.P. Steele, J. Phys. Chem. A **119**(50), 12119 (2015)
71. Z. Long, A.O. Atsango, J.A. Napoli, T.E. Markland, M.E. Tuckerman, J Phys Chem Lett **11**(15), 6156 (2020)
72. S.W. Rick, S.J. Stuart, B.J. Berne, J. Chem. Phys. **101**(7), 6141 (1994)
73. P. Zhang, N. Zhang, Y. Deng, D. Bluestein, J. Comput. Phys. **284**, 668 (2015)
74. J. Behler, M. Parrinello, Phys. Rev. Lett. **98**, 146401 (2007)
75. T. Vlaar, B. Leimkuhler, arXiv:2106.10771 [cond-mat, physics:physics] (2021)
76. C. Han, P. Zhang, D. Bluestein, G. Cong, Y. Deng, J. Comput. Phys. **427**, 110053 (2021)
77. E. Krieger, G. Vriend, J. Comput. Chem. **36**(13), 996 (2015)
78. Y. Liu, M.E. Tuckerman, J. Chem. Phys. **112**(4), 1685 (2000)